Available online at www.sciencedirect.com

ScienceDirect

Trans. Nonferrous Met. Soc. China 35(2025) 157−168

Transactions of
Nonferrous Metals
Society of China

www.tnmsc.cn

Influence of laser shock peening on microstructure and high-temperature oxidation resistance of Ti45Al8Nb alloy fabricated via laser melting deposition

Lu-lu JIANG[1], Liang LAN[1], Cheng-yan BAI[1], Ru-yi XIN[1],
Shuang GAO[1], Hao-yu WANG[1], Bo HE[1], Chao-yue CHEN[2], Guo-xin LU[3]

1. Research Center of High-Temperature Alloy Precision Forming, School of Materials Science and Engineering,
Shanghai University of Engineering Science, Shanghai 201620, China;
2. State Key Laboratory of Advanced Special Steels, School of Materials Science and Engineering,
Shanghai University, Shanghai 200444, China;
3. School of Materials Science and Engineering, Shandong University, Jinan 250061, China

Received 1 July 2023; accepted 28 December 2023

Abstract: Laser shock peening (LSP) was used to enhance the high-temperature oxidation resistance of laser melting deposited Ti45Al8Nb alloy. The microstructure and high-temperature oxidation behavior of the as-deposited Ti45Al8Nb alloy before and after LSP were investigated by scanning electron microscopy, X-ray diffraction, and electron backscatter diffraction. The results indicated that the rate of mass gain in the as-deposited sample after LSP exhibited a decrease when exposed to an oxidation temperature of 900 °C, implying that LSP-treated samples exhibited superior oxidation resistance at high temperatures. A gradient structure with a fine-grain layer, a deformed-grain layer, and a coarse-grain layer was formed in the LSP-treated sample, which facilitated the diffusion of the Al atom during oxidation, leading to the formation of a dense Al_2O_3 layer on the surface. The mechanism of improvement in the oxidation resistance of the as-deposited Ti45Al8Nb alloy via LSP was discussed.

Key words: TiAl alloy; laser melting deposition; laser shock peening; additive manufacturing; oxidation resistance

1 Introduction

TiAl-based alloys are used extensively in the low-pressure turbine blades of air turbine engines and exhaust valves of automotive engines with the characteristics of low densities, high elastic modulus, and high melting point [1−4]. Laser melting deposition (LMD) as an attractive additive manufacturing (AM) technology, has been increasingly appropriate for the manufacture of TiAl alloys because of its low cost, high speed and rapid solidification [5−8]. Compared with the laser powder bed fusion process, the TiAl alloy prepared by LMD has less residual stress and fewer cracks. Nevertheless, the limited oxidation resistance for TiAl alloys at high temperatures (exceeding 800 °C) acts as a barrier to their widespread utilization [9]. Conventional methods of synthesizing protective coatings, such as MCrAlY, NiCoCrAlY, SiO_2, Al_2O_3 and Cr_2O_3, have been used to improve oxidation resistance [10−15]. The implementation of an oxide stratum or the facilitation of oxide stratum generation has the role of a formidable bulwark, impeding the permeation of oxygen or other deleterious agents into substrate. This fortification

---

Corresponding author: Liang LAN, Tel: +86-21-67796016, E-mail: lanliang@sues.edu.cn;
Bo HE, Tel: +86-21-67796017, E-mail: hebo@sues.edu.cn

https://doi.org/10.1016/S1003-6326(24)66671-9

shields the foundational material from the perils of oxidation or corrosion. However, the synthetic methods of traditional protective coatings are limited by inadequate chemical compatibility, substantial interdiffusion and weak mechanical performances. Additionally, the bonding between the coating and the substrate is feeble, posing difficulties in meeting the thermal cycle demands.

Laser shock peening (LSP) is a competitive surface treatment method that enhances the mechanical performances of metallic parts [16−20]. Different from traditional shot peening, LSP generates severe plastic deformation with an ultrahigh strain rate on the material's surface, resulting in a deeper depth of the affected layer and higher residual compressive stress. Thus, it improves microhardness, fatigue strength and oxidation resistance of the metallic parts via inducing deep compressive residual stress, fine grains and surface hardening. LUO et al [21] reported that the laser AM TC17 specimen after LSP treatment exhibited more excellent fatigue strength in comparison to the as-prepared specimen. Our previous results showed that the fatigue strength of electron beam powder bed fusion processed Ti6Al4V alloy was increased by 17% after LSP treatment [22]. LU et al [23] found that LSP modified the thermal corrosion performance of the Ti6Al4V alloy part formed by laser powder bed fusion (LPBF) due to the formation of plenty of nanotwins and high-density dislocations during LSP. GUO et al [24] researched the influence of LSP on the high-temperature oxidation resistance of Ti6Al4V sample fabricated through laser AM, and found that the mass gain rate of the sample at oxidation temperature of 700 °C was reduced by 34% through LSP. WANG et al [25] further evaluated the role of annealing heat treatment in oxidation resistance of LPBF-processed Ti6Al4V sample with LSP at 700 °C. However, there is less research work related to the effect of LSP on the oxidation behavior of additively manufactured TiAl alloys, especially for the Ti45Al8Nb alloys prepared via LMD process. In addition, the mechanism of the improvement in oxidation resistance above 800 °C for LMD-prepared Ti45Al8Nb alloy treated by LSP has not yet been investigated systematically, severely limiting the application of high-Nb TiAl alloy in high-temperature environments.

Consequently, the aim of this work is to explore the high-temperature oxidation resistance of LMD-prepared Ti45Al8Nb alloy through LSP treatment. The microstructure, phase composition and oxidation behaviors of the as-prepared Ti45Al8Nb alloys at high temperature of 900 °C before and after LSP were investigated. The influence mechanism of LSP on the oxidation resistance of the as-prepared Ti45Al8Nb alloy was revealed. This study will provide a theoretical reference for AM TiAl alloy components in high-temperature engineering applications.

2 Experimental

2.1 Materials and samples preparation

Ti45Al8Nb pre-alloying powder, prepared via plasma rotation electrode process, was utilized as the deposition raw material, and its composition is illustrated in Table 1. The Ti45Al8Nb samples were fabricated by the LMD equipment. The process parameters were set as follows: scanning speed of 9 mm/s, laser power of 1400 W, average layer thickness of 0.4 mm, beam diameter of 3 mm, powder feeding of 8.4 g/min and gas flow rates of 8 L/min. After the preparation, the samples underwent a heat treatment process at 950 °C for 4 h in a tubular heating furnace to reduce residual stress. The material was cut into small pieces (10 mm × 10 mm × 3 mm) for LSP treatment. LSP was applied to both two sides (10 mm × 10 mm) of the samples. During LSP, an Nd:YAG laser system with a wavelength of 1.064 μm was employed, and the parameters were as follows: laser energy of 9 J, laser beam diameter of 2.5 mm, laser pulse duration time of 12 ns, repetition rate of 1 Hz, and overlapping rate of 25%, laser power density of 15.28 GW/cm^2. The specimens were protected using the absorbing and water-spraying layers.

Table 1 Chemical composition of Ti45Al8Nb powder (wt.%)

Al	Nb	Fe	N	O	H	C	Ti
29.46	17.41	0.06	0.004	0.068	0.001	0.014	Bal.

2.2 Oxidation tests

The specimens underwent ultrasonic cleaning utilizing acetone and were subsequently immersed in anhydrous ethanol prior to oxidation tests. Isothermal oxidation experiments were conducted in a resistance furnace in static air at 900 °C for a duration of 200 h. A schematic illustration of oxidation tests of LSP-treated samples is demonstrated in Fig. 1. The sample was placed obliquely in a cylindrical corundum crucible to ensure that all surfaces were thoroughly exposed to the air during the oxidation experiment. The crucibles containing the samples were placed in a furnace and started the oxidation experiment. The samples were cooled to room temperature after 1, 4, 7, 10, 20, 30, 100, 120, 140, and 200 h. After reaching room temperature, an electronic balance with a precision of ±0.1 mg was employed to measure their mass. For each oxidation condition, the average mass of three samples was selected.

2.3 Microstructural characterization

The microstructures of the specimens before and after LSP were analyzed by means of optical microscopy (OM), scanning electron microscopy (SEM) and electron backscatter diffraction (EBSD). After the oxidation, SEM was used to observe the oxidation layer structure and surface morphology of the samples. Energy disperse spectroscopy (EDS) was used to determine the element distribution in the cross-section of the oxidation layer. The EBSD scans were performed on a field emission gun-SEM Zeiss Gemini 450 equipped with a NordlysMax3 EBSD camera at an accelerating voltage of 20 kV, beam current of 20 nA, and step size of 0.2 μm. Samples were prepared by electrolytic polishing using 10% perchloric acid, 30% ethylene glycol, and 60% methanol. The phases analysis on the oxidation surface was performed using X-ray diffraction (XRD) with a Cu K_α radiation source. The residual stresses on the surface of the samples before and after LSP were assessed using XRD method.

3 Results

3.1 Microstructure

Figure 2 presents OM and SEM images of Ti45Al8Nb samples fabricated via LMD. Plenty of γ/α_2 lamellae and a few pores were observed in Fig. 2(a). A slice of the lamellar grains showed typical columnar morphology and was called columnar lamellar grains [26]. Figure 2(b) shows a higher magnification image of γ/α_2 lamellar colonies. The grain boundaries of the γ/α_2 lamellae were relatively straight, and equiaxed γ grains could be observed at the colony boundaries. Additionally, discontinuous coarsening was observed in γ/α_2 lamellar grains, which was attributed to the enrichment of Al element at the tip of γ lamella, resulting in a eutectic reaction [27]. Figure 3 shows XRD patterns of as-deposited Ti45Al8Nb samples before and after LSP. In Fig. 3, the as-deposited Ti45Al8Nb alloy mainly contained α_2-Ti_3Al phase and γ-TiAl phase, and no new phase was found after LSP treatment.

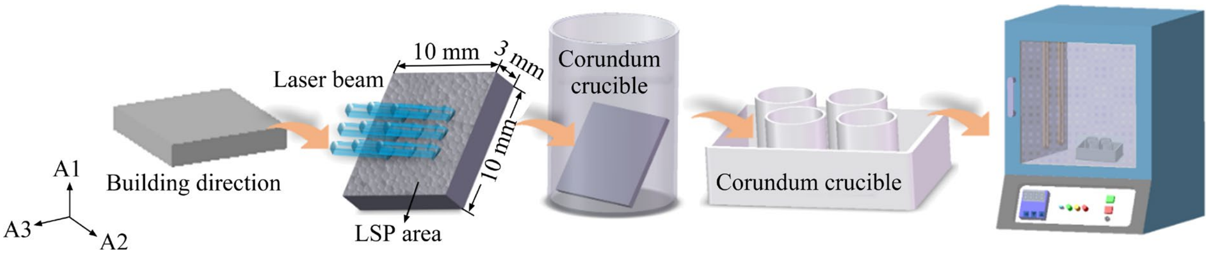

Fig. 1 Schematic illustration of oxidation tests of LSP-treated samples

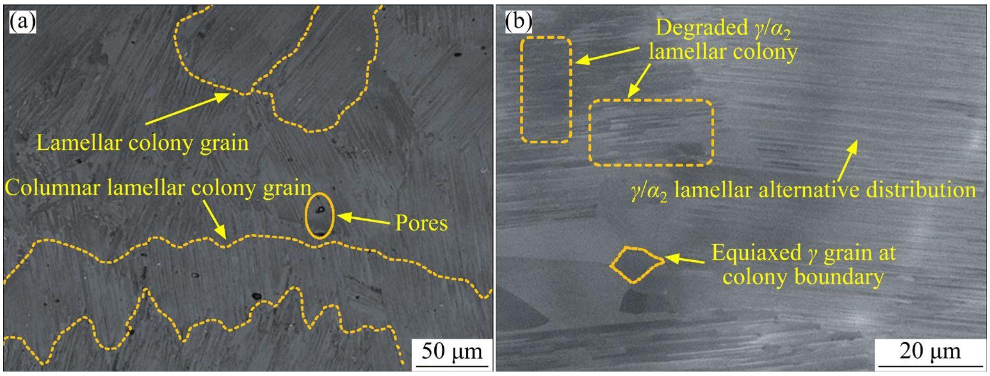

Fig. 2 OM (a) and SEM (b) images of LMD-prepared Ti45Al8Nb samples

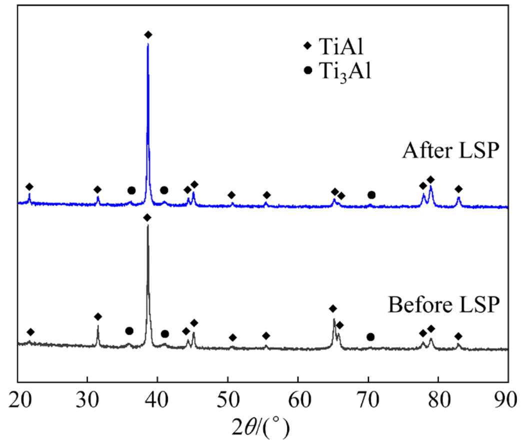

Fig. 3 XRD patterns of LMD-prepared Ti45Al8Nb samples before and after LSP

EBSD analysis was performed on the cross-section of the samples, and could qualitatively describe the morphology, size and boundaries of the grains before and after LSP, as shown in Fig. 4. Figure 4(a) shows γ/α_2 lamellar structure in the LMD-prepared Ti45Al8Nb samples before LSP. Clearly, a gradient structure was generated on the surface of the sample treated with LSP, as depicted in Fig. 4(b). Microstructural characteristics from Fig. 4(b) suggested that the LSP-treated sample could be segregated into three regions from the surface layer to the internal layer, namely the surface fine-grain layer, the deformed-grain layer, and the coarse-grain layer. From Fig. 4(c), the average grain size of γ/α_2 lamellae in the as-deposited sample was 44.93 μm, while the average grain size in the LSP-treated sample was 16.75 μm. This indicated significant grain refinement in the LMD-prepared Ti45Al8Nb samples subjected to LSP treatment. Figures 4(d−f) show the grain boundary distribution of the LMD-prepared Ti45Al8Nb samples before and after LSP. It was observed that the proportion of low-angle grain boundaries in the LSP samples was larger than that in the as-deposited samples, which showed that LSP effectively enhanced grain boundaries and refined the grains, resulting in the formation of sub-grain boundaries.

Figure 5 presents the pole figures of γ and α_2 phases in as-deposited Ti45Al8Nb samples before and after LSP. From Fig. 5, the texture intensity of γ-TiAl phase decreased from 58.35 to 37.48, and that of α_2-Ti_3Al phase decreased from 61.06 to 19.92 after LSP, implying that the texture intensity in the as-deposited sample was weakened via LSP. SUN et al [28] found that the decrease of texture intensity in Ti-17 titanium alloy after LSP was due to random grain rotation under the interaction between the shock wave and material. In addition, α_2 and γ were in line with the Blackburn relationship for as-deposited Ti45Al8Nb alloy before and after LSP: $\{0001\}_{\alpha_2}//\{111\}_{\gamma}$ and $\{11\bar{2}0\}_{\alpha_2}//\{110\}_{\gamma}$. The result was also reported by MA et al [29].

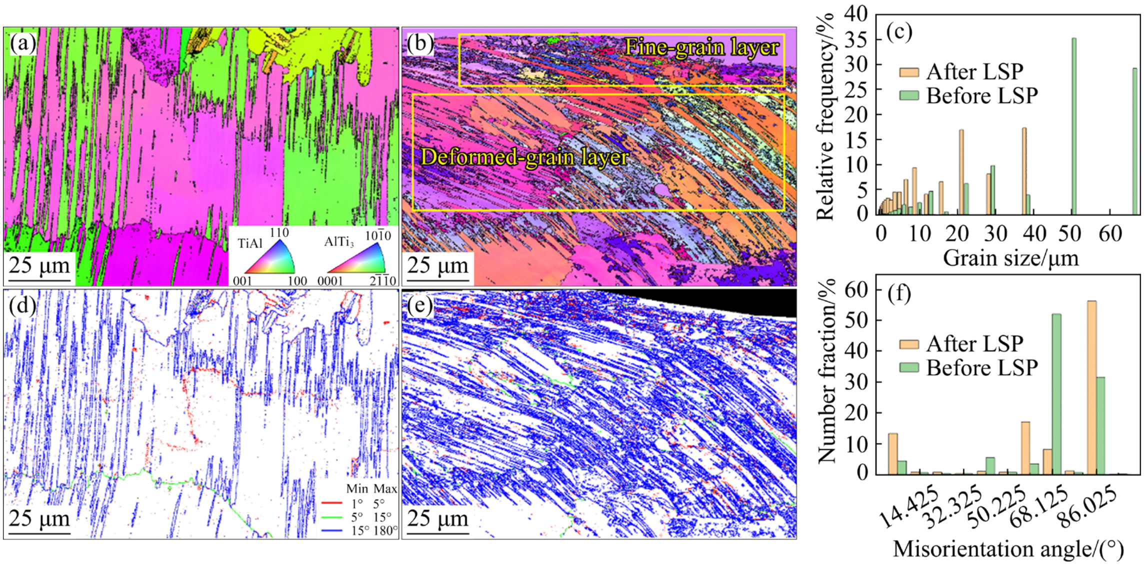

Fig. 4 EBSD maps of LMD-prepared Ti45Al8Nb sample: (a) Inverse pole figure of sample before LSP; (b) Inverse pole figure of sample after LSP; (c) Grain size distribution; (d) Grain boundary map of sample before LSP; (e) Grain boundary map of sample after LSP; (f) Misorientation angle distribution histogram

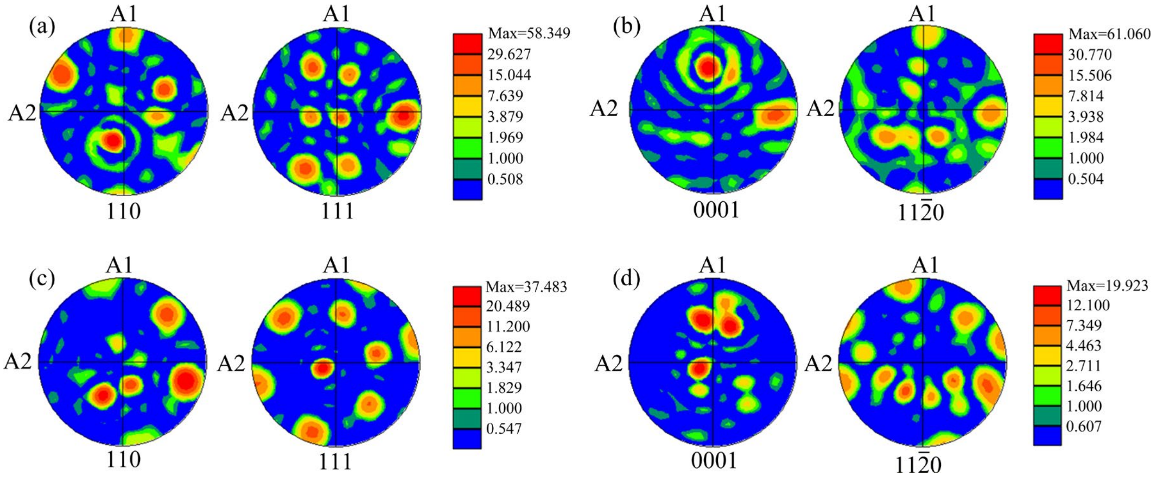

Fig. 5 Pole figures of LMD-prepared Ti45Al8Nb sample before (a, b) and after (c, d) LSP: (a, c) γ-TiAl phase; (b, d) α_2-Ti_3Al phase

3.2 Oxidation behaviors at high temperature

The oxidation kinetics profiles of LMD-deposited samples before and after LSP at 900 °C for 200 h are illustrated in Fig. 6. The overall trend of the oxidation kinetic curves for both samples was similar with a gradual increase in mass. Although the difference in mass gain was not significant for the two samples in the initial oxidation stage, the increase in mass for LSP samples was less in comparison to the as-deposited ones as the oxidation time progressed. K_n (rate constant) of the as-deposited samples after 200 h was almost twice that of the LSP-treated samples. During the oxidation process, the surface peeling in the as-prepared samples was more serious than that in the LSP-treated samples. Therefore, the more complete oxidation layer after LSP provided better protection for the matrix.

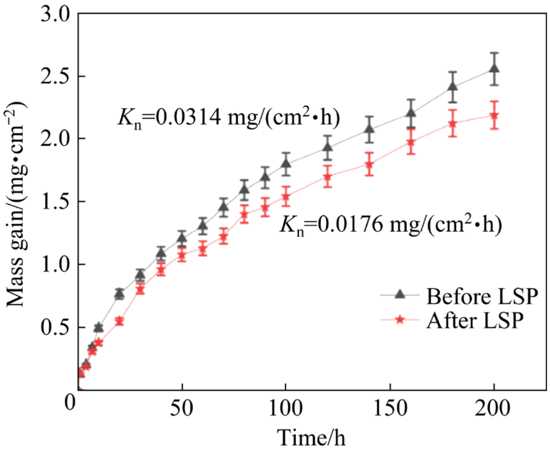

Fig. 6 Oxidation kinetics curves of LMD-prepared Ti45Al8Nb samples at 900 °C for 200 h

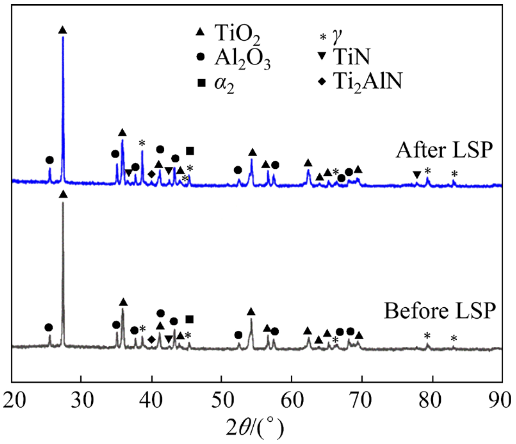

Fig. 7 XRD patterns of surface after oxidation at 900 °C for 200 h before and after LSP

Figure 7 shows XRD patterns at oxidation temperature of 900 °C for 200 h before and after LSP. For as-deposited samples after oxidation, the phase peaks were mainly composed of TiO_2, Al_2O_3, α_2-Ti_3Al, γ-TiAl, TiN, and Ti_2AlN phases. Notably, the absence of any new diffraction peaks through LSP indicated that the phase composition remained unchanged during the oxidation process. However, the peak intensity of Al_2O_3 was slightly enhanced in the LSP-treated samples. This contributed to the formation of a continuous oxide film that served as a protective shield, preventing the reaction between oxygen and the substrate. Figure 8 shows the cross-sectional images and EDS profiles of the as-prepared Ti45Al8Nb samples before and after LSP during oxidation at 900 °C for 200 h. From Figs. 8(a, c), the oxide film on the as-deposited samples consisted of an inner oxide layer and outer oxide layer, with Al and Ti distribution in a complementary trend along the direction from the inside to the outer. The EDS results indicated that the composition of the outer oxide layer was primarily TiO_2, and the inner oxide layer consisted of TiO_2 and Al_2O_3 for as-deposited samples. Moreover, a slice of cracks could be clearly observed in the as-deposited sample rather than in the LSP-treated sample. After LSP, Al_2O_3 oxide film containing TiO_2 was found in the outer oxide layer, as shown in Figs. 8(b, d), which implied that a larger number of Al diffused into the outer oxide layer and underwent a reaction with oxygen, resulting in the formation of Al_2O_3. Additionally, the oxide film thickness of the LSP-treated samples was reduced by 25% compared to the as-deposited samples. An Nb-rich layer was observed on the oxide film for as-deposited samples before and after LSP.

Figure 9 presents the surface morphology of the oxide scale of the as-deposited Ti45Al8Nb samples before and after LSP oxidized at 900 °C for varying durations. Table 2 gives the EDS analysis results of the oxide particulates of Fig. 9 at 900 °C for 200 h. The surface oxide scale of as-prepared samples was relatively uniform and neat in Figs. 9(a−c). The oxides of LSP samples were relatively tighter and smaller in Figs. 9(d−f). After 100 h, raised cluster oxides and small raised white bright oxides appeared in the LSP samples. Based on the EDS analysis results in Table 2, the composition of surface oxides was both Al_2O_3 and

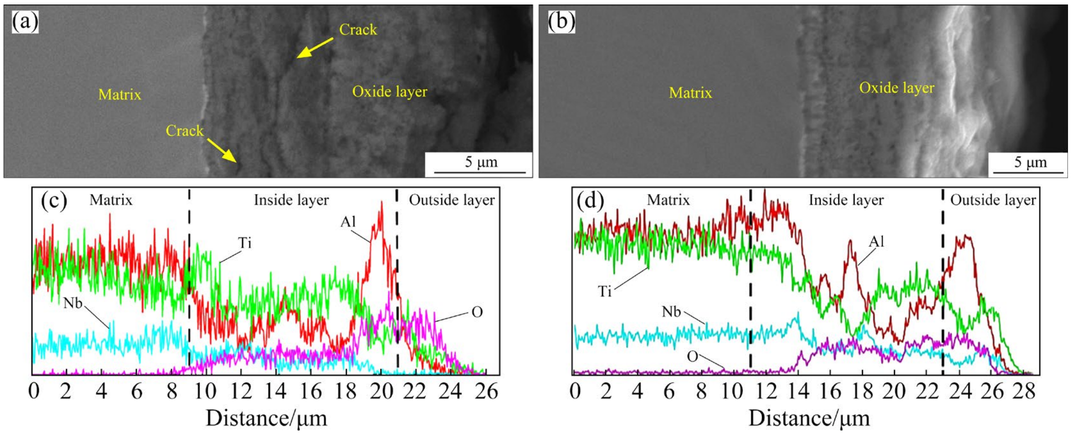

Fig. 8 Cross-sectional morphologies (a, b) and EDS profiles (c, d) in as-deposited sample after oxidation at 900 °C for 200 h: (a, c) Before LSP; (b, d) After LSP

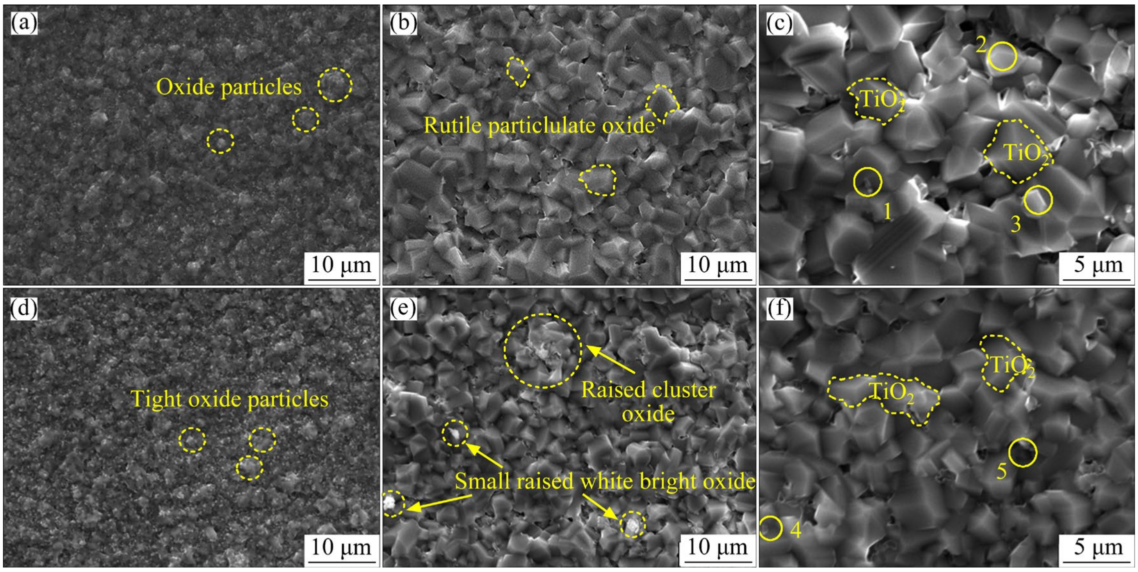

Fig. 9 SEM images of oxide scale on surface of as-deposited (a−c) and LSP-treated (d−f) samples after oxidation at 900 °C for different time: (a, d) 10 h; (b, e) 100 h; (c, f) 200 h

Table 2 Chemical composition at various points indicated in Fig. 9 for as-deposited and LSP-treated samples oxidized at 900 °C for 200 h (at.%)

Sample	Point No.	Ti	Al	O	Others
Before LSP	1	11.96	19.19	68.17	0.23
	2	23.65	0.06	76.05	0.24
	3	21.22	0.91	77.70	0.17
After LSP	4	32.53	28.16	39.12	0.19
	5	14.11	35.16	50.56	0.17

TiO_2, but LSP-treated samples exhibited finer oxide particles. The average size of oxide particles at 900 °C for 100 and 200 h before and after LSP is shown in Fig. 10. The oxide particles grew with increasing the holding time. The oxide particle sizes of the LSP-treated specimens were smaller than those of the as-prepared specimens at 900 °C.

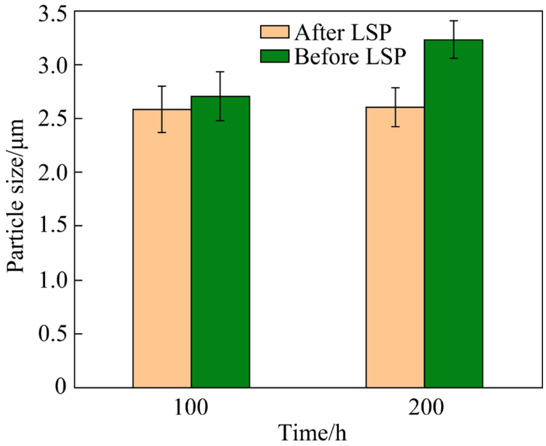

Fig. 10 Average size of oxide particles on surfaces of as-deposited and LSP-treated Ti45Al8Nb samples at 900 °C for 100 and 200 h

4 Discussion

4.1 Effect of LSP on microstructure

According to the microstructure analysis in Section 3.1, LSP treatment clearly refined the grains of the as-deposited Ti45Al8Nb samples. A gradient structure containing the fine-grain layer, the deformed-grain layer, and the coarse-grain layer along the depth direction, was formed in the LSP-treated samples. Previous studies [23,30] indicated that the grain refinement underwent a series of dislocation evolution, commencing with dislocation tangles and progressing to dislocation cells. Subsequently, the process continued with the formation of subgrains, culminating in the achievement of refined grains. During the initial stages of deformation under LSP, dislocation slip predominantly contributed to the deformation of γ/α_2 grains in the as-deposited samples. With the accumulation of the dislocations in γ/α_2 grains, dislocation tangles, dislocation networks, and dislocation cells gradually appeared, leading to the formation of subgrains. And then, some subgrains transformed into new grains through dynamic recrystallization. With the increase of depth, the deformed-grain layer was formed on the subsurface while the gradual weakening of the peak pressure of shock wave occurred. Furthermore, LSP was widely recognized as an adiabatic process due to its exceptional strain rate, which triggered a rise in temperature by converting plastic deformation into heat [31−33]. In the present study, the adiabatic temperature in the as-deposited Ti45Al8Nb samples through LSP was calculated as ~1087 K, which was higher than the recrystallization temperature of $0.4T_m$. Consequently, the adiabatic temperature triggered through LSP afforded the thermal driving force for dynamic recrystallization [34]. Dynamic recrystallization helped to refine the grain and therefore enhanced the oxidation resistance of the alloy.

The main phase of the as-deposited Ti45Al8Nb sample before and after LSP is γ-TiAl, and the content of Ti_3Al phase was very small, as shown in Fig. 3. Figure 11 shows the EBSD Schmid factor maps for γ-TiAl on slip and twining systems. Red, green and blue show high, medium and low Schmid factor values. Deformation twinning and dislocation slip were both competing modes of plastic deformation of crystalline materials [35]. The γ-TiAl had low symmetry and few slip systems, and mainly $\{111\}\langle110\rangle$ slip systems. From Fig. 11(a, b), there was little change for Schmid factor values of the $\{111\}\langle110\rangle$ systems before and after LSP, so the plastic deformation was conducted in deformation twinning with a system of $\{111\}\langle112\rangle$ during LSP. It was observed that the $\{111\}\langle112\rangle$ twinning systems possessed high Schmid factor values after LSP, as shown in Figs. 11(c, d). This meant that most grain deformation occurred through twinning during LSP. ZHANG et al [36] reported that deformation twinning was activated in Ti−47Al−2Cr−2Nb alloy fabricated through direct laser deposition under tensile loading. Therefore, a gradient structure of

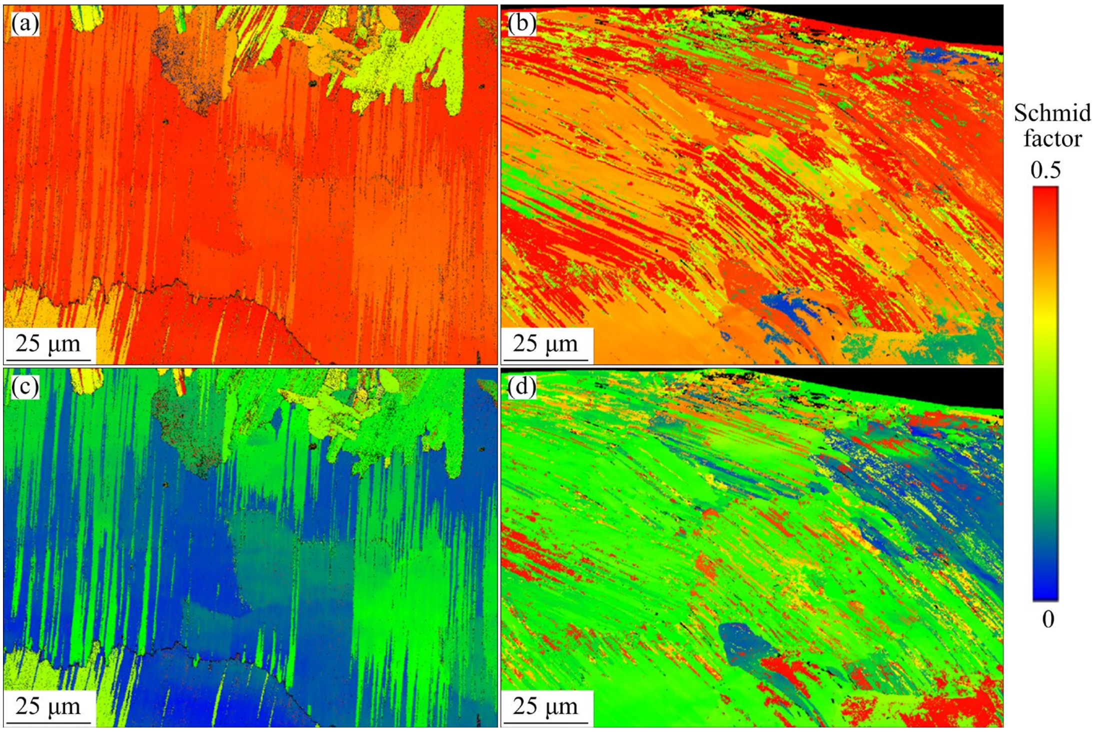

Fig. 11 Schmid factor maps of *γ* phase in as-deposited Ti45Al8Nb sample before (a, b) and after (c, d) LSP: (a, c) {111}⟨110⟩ slip; (b, d) {111}⟨112⟩ twinning system

the as-deposited sample after LSP consisted of a refined-grain layer, a deformed layer and a coarse-grain layer.

4.2 Oxidation resistance at high temperature

As mentioned in Section 3.2, the LMD-prepared Ti45Al8Nb alloy after LSP treatment showed outstanding oxidation resistance, which could be ascribed to the excellent adhesion of the oxide film. During the early stage of oxidation, O_2 underwent decomposition into O atoms and then reacted with active Ti, thus inducing a TiO_2 oxide layer with a certain thickness on the surface because of the faster diffusion rate of Ti atom. According to Ellingham−Rechardson diagram, the equilibrium oxygen pressure of Al_2O_3/Al at 900 °C was apparently lower than that of M_xO_y/M (M for Nb, Cr, Mn and other sub-group elements) [37]. As the oxidation time increased, Al diffused outward by the loose TiO_2 layer and reacted with oxygen to form an Al_2O_3 oxide layer. Thus, the oxide scale of Ti45Al8Nb alloy exhibited a multilayer structure consisting of TiO_2+Al_2O_3 mixed layer, and TiO_2 from inside to outside. Additionally, an Nb-rich layer was found between the oxide film and matrix, which was the representative characteristic of the high-Nb TiAl alloy during oxidation [38,39].

After LSP, grain refinement affected the high-temperature oxidation performance of the LMD-prepared Ti45Al8Nb alloy. Firstly, a gradient structure composed of a fine-grains layer and high-density dislocations was formed in LSP-treated sample. The gradient structure facilitated the diffusion of Al on the surface, resulting in the formation of a compact Al_2O_3 protective layer. It was observed in Fig. 8 that the samples exhibited more Al_2O_3 layers after LSP. And a dense, continuous oxide layer could prevent the specimen from further oxidation. CAO et al [40] pointed out that the high-temperature oxidation resistance of Ni-based superalloy GH202 via LSP was enhanced due to the formation of a denser oxidation scale of Cr_2O_3. Notably, LSP refined the grains on the surface, resulting in fine oxidation particles. The oxide particles of the samples after LSP were smaller than those of the samples before LSP, as shown in Fig. 10, indicating that the degree of oxidation of the samples after LSP was low. Because LSP increased the activation energy required for the oxidation of the as-deposited Ti45Al8Nb alloy, more energy was required for the progress of the oxidation reaction. Furthermore, the compressive residual stress induced during LSP was beneficial to obtaining the oxide film integrity without cracking and spallation. It was well known that high residual compressive stresses were generated on the surface of additively manufactured parts during LSP [41,42]. As shown in Fig. 12, the residual compressive stress of −471 MPa was formed on the surface of the as-deposited sample after LSP. The existence of residual compressive stress restrained crack generation, contributing to the development of a denser oxide layer without defects on the surface layer. As shown in Fig. 8, the oxide scale showed no cracking in the LSP-treated samples, while cracking was observed in the as-deposited samples. CHEN et al [18] also reported that the residual compressive stress can improve high-temperature oxidation resistance of the Ni-based superalloy. Moreover, the residual compressive stress of LSP-treated after oxidation at 900 °C was −53 MPa, indicating that the residual compressive stress was almost relaxed. It was attributed to the rapid annihilation and recombination of dislocations via short-range diffusion during the isothermal oxidation process. Moreover, the growth of refined grains for a long exposure depletes the stored energy within deformed metal, leading to a gradual dissipation of the residual stress throughout oxidation [43].

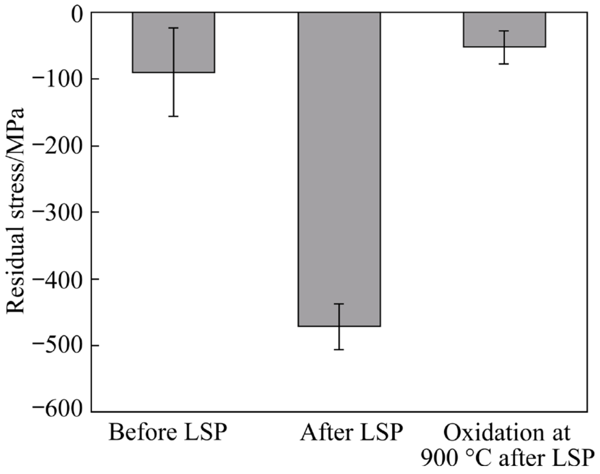

Fig. 12 Residual stress on surface of samples before and after LSP

Based on the above analysis, the influence mechanism of LSP on the oxidation behaviors of the LMD-prepared Ti45Al8Nb alloy is shown schematically in Fig. 13. Before LSP, an uneven loose oxide layer with some cracks was formed in the as-deposited sample. However, a dense uniform oxide layer with relatively finer grains was induced on the surface of LSP-treated alloy, which prevented further oxidation of the matrix, and thus improving the high-temperature oxidation resistance of the LMD-prepared Ti45Al8Nb alloy.

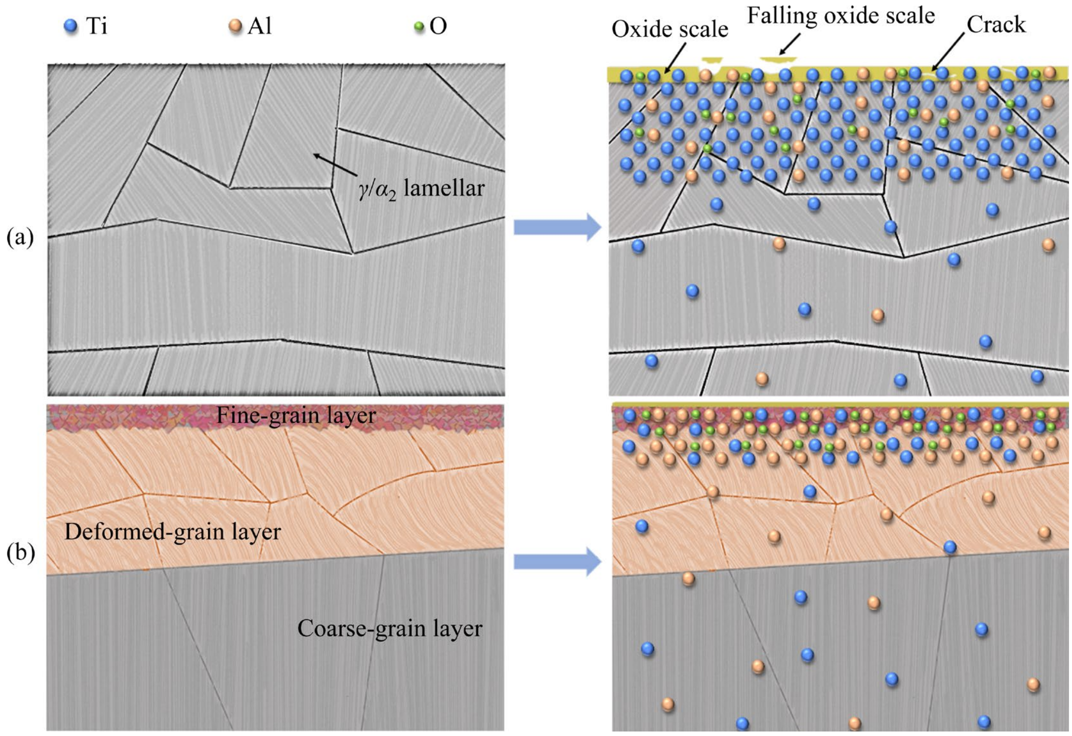

Fig. 13 Schematic illustration of oxidation process for as-deposited (a) and LSP-treated (b) samples

5 Conclusions

(1) The microstructure analysis showed that the grains in as-deposited sample were clearly refined subjected to LSP treatment. A gradient structure containing the fine-grain layer, the deformed-grain layer, and the coarse-grain layer was induced in the LSP-treated sample.

(2) In comparison to the as-deposited sample, the LSP-treated samples possessed a decreased rate of mass gain at an oxidation temperature of 900 °C for 200 h, showing that LSP treatment significantly improved the oxidation resistance of the as-deposited sample at high temperature.

(3) The EDS results showed an Nb-rich layer was observed on the oxide film of as-deposited sample before and after LSP, and the oxide scale thickness after LSP was reduced by 25%. Additionally, LSP reduced the particle size in the oxide scale.

(4) The mechanism of LSP to improve the oxidation resistance of the as-deposited alloy was revealed. The effects of the gradient structure and compressive residual stress induced via LSP led to dense uniform oxide film with relatively finer grains, thereby improving the oxidation resistance of the as-deposited Ti45Al8Nb alloy at high temperature.

CRediT authorship contribution statement

Lu-lu JIANG: Data curation, Formal analysis, Investigation, Writing − Original draft; **Liang LAN:** Conceptualization, Data curation, Formal analysis, Investigation, Supervision, Resources, Writing − Review & editing; **Cheng-yan BAI:** Formal analysis; **Ru-yi XIN**: Investigation, Data curation; **Shuang GAO:** Formal analysis; **Hao-yu WANG:** Investigation, Formal analysis; **Bo HE:** Funding acquisition, Writing − Review & editing; **Chao-yue CHEN:** Investigation, Resources; **Guo-xin LU**: Resources.

Declaration of competing interest

The authors declare that they have no known competing financial interests or personal relationships that could have appeared to influence the work reported in this paper.

Acknowledgments

This work was supported by the Class III Peak Discipline of Shanghai, China—Materials Science and Engineering (High-Energy Beam Intelligent Processing and Green Manufacturing).

References

[1] XUE Hui, LIANG Yong-feng, PENG Hui, WANG Yan-li, LIN Jun-pin. Additive manufacturing of micro/nano multiphase synergistically reinforced Ti−55Al−7.5Nb with a reticular boundary precipitate via direct laser deposition [J]. Additive Manufacturing, 2022, 58: 102989.

[2] XU Run-run, LI Miao-quan. Quantitative characterization of *β*-solidifying *γ*-TiAl alloy with duplex structure [J]. Transactions of Nonferrous Metals Society of China, 2021, 31: 1993−2004.

[3] SUN Tie-long, LIANG Yong-feng, YANG Gang, GUO Zhi-chao, CAO Jun, MU Yan-xun, LIN Jun-pin. Twinning behavior and strengthening mechanism in a microalloyed TiAl alloy [J]. Materials Science and Engineering A, 2023, 872: 144993.

[4] LIU Zhan-qi, MA Rui-xin, XU Guo-jian, WANG Wen-bo, SU Yun-hai. Effects of annealing on microstructure and mechanical properties of *γ*-TiAl alloy fabricated via laser melting deposition [J]. Transactions of Nonferrous Metals Society of China, 2020, 30: 917−927.

[5] ZHANG D, QIU D, GIBSON M A, ZHENG Y, FRASER H L, STJOHN D H, EASTON M A. Additive manufacturing of ultrafine-grained high-strength titanium alloys [J]. Nature, 2019, 576: 91−95.

[6] HUANG Dan-ni, TAN Qi-yang, ZHOU Ying-hao, YIN Yu, WANG Feng, WU Tao, YANG Xian-liang, FAN Zhi-qi, LIU Yin-gang, ZHANG Jing-qi, HUANG Han, YAN Ming, ZHANG Ming-xing. The significant impact of grain refiner on *γ*-TiAl intermetallic fabricated by laser-based additive manufacturing [J]. Additive Manufacturing, 2021, 46: 102172.

[7] ZHAO Rui-xin, CHEN Chao-yue, SHUAI San-san, HU Tao, FAUTRELLE Y, LIAO Han-lin, LU Jian, WANG Jiang, REN Zhong-ming. Enhanced mechanical properties of Ti6Al4V alloy fabricated by laser additive manufacturing under static magnetic field [J]. Materials Research Letters, 2022, 10: 530−538.

[8] BAI Cheng-yan, LAN Liang, XIN Ru-yi, GAO Shuang, HE Bo. Microstructure evolution and cyclic deformation behavior of Ti−6Al−4V alloy via electron beam melting during low cycle fatigue [J]. International Journal of Fatigue, 2022, 159: 106784.

[9] RITTINGHAUS S K, WILMS M B. Oxide dispersion strengthening of *γ*-TiAl by laser additive manufacturing [J]. Journal of Alloys and Compounds, 2019, 804: 457−460.

[10] KONG Ling-yan, QI Jian-zhong, LU Bin, YANG Rui, CUI Xin-yu, LI Tie-fan, XIONG Tian-ying. Oxidation resistance of TiAl3−Al composite coating on orthorhombic Ti2AlNb based alloy [J]. Surface and Coatings Technology, 2010, 204: 2262−2267.

[11] WANG Q M, ZHANG K, GONG J, CUI Y Y, SUN C, WEN L S. NiCoCrAlY coatings with and without an Al_2O_3/Al interlayer on an orthorhombic Ti_2AlNb-based alloy: Oxidation and interdiffusion behaviors [J]. Acta Materialia,

2007, 55: 1427−1439.

[12] WU Lian-kui, WU Jing-jia, WU Wei-yao, CAO Fa-he, JIANG Mei-yan. Sol−gel-based coatings for oxidation protection of TiAl alloys [J]. Journal of Materials Science, 2020, 55: 6330−6351.

[13] TANG Zhao-lin, WANG Fu-hui, WU Wei-tao. Effect of a sputtered TiAlCr coating on the oxidation resistance of TiAl intermetallic compound [J]. Oxidation of Metals, 1997, 48: 551−525.

[14] PFLUMM R, FRIEDLE S, SCHÜTZE M. Oxidation protection of γ-TiAl-based alloys — A review [J]. Intermetallics, 2015, 56: 1−14.

[15] TIAN Yu-xin, XIAO Hua-qiang, YOU Chuan-chuan, FENG Jin-yu, XIAO Yi, ZHOU Xuan. High-temperature oxidation and wear properties of laser cladded Ti−Al−N composite coatings [J]. Transactions of Nonferrous Metals Society of China, 2023, 33: 1779−1791.

[16] WEI Bo-xin, XU Jin, FRANK CHENG Y, WU Jia-jun, SUN Cheng, WANG Zhen-yao. Microstructural response and improving surface mechanical properties of pure copper subjected to laser shock peening [J]. Applied Surface Science, 2021, 564: 150336.

[17] YANG H F, XIONG F, WANG Y, JIA L, LIU H, HAO J B. Manufacturing profile-free copper foil using laser shock flattening [J]. International Journal of Machine Tools and Manufacture, 2020, 152: 103542.

[18] CHEN Lan, SUN Yu-zhou, LI Lin, REN Xu-dong. Improvement of high temperature oxidation resistance of additively manufactured TiC/Inconel 625 nanocomposites by laser shock peening treatment [J]. Additive Manufacturing, 2020, 34: 101276.

[19] HE Dong-sheng, LI Liu-he, GUO Wei, HE Guang-zhi, PENG Peng, SHAO Tian-wei, HUAN Heng, ZHANG Gong-xuan, HAN Guo-feng, YAN Jian-feng. Improvement in oxidation resistance of Ti_2AlNb alloys at high temperatures by laser shock peening [J]. Corrosion Science, 2021, 184: 109364.

[20] YE Yi-xuan, ZHANG Yu, HUANG Tao, ZOU Shi-kun, DONG Ya-lin, DING Han, VASUDEVAN V K, YE Chang. A critical review of laser shock peening of aircraft engine components [J]. Advanced Engineering Materials, 2023, 25: 103642.

[21] LUO Si-hai, HE Wei-feng, CHEN Kai, NIE Xiang-fan, ZHOU Liu-cheng, LI Yi-ming. Regain the fatigue strength of laser additive manufactured Ti alloy via laser shock peening [J]. Journal of Alloys and Compounds, 2018, 750: 626−635.

[22] JIN Xin-yuan, LAN Liang, GAO Shuang, HE Bo, RONG Yong-hua. Effects of laser shock peening on microstructure and fatigue behavior of Ti−6Al−4V alloy fabricated via electron beam melting [J]. Materials Science and Engineering A, 2020, 780: 139199.

[23] LU Hai-fei, WANG Zhao, CAI Jie, XU Xiang, LUO Kai-yu, WU Liu-jun, LU Jin-zhong. Effects of laser shock peening on the hot corrosion behaviour of the selective laser melted Ti6Al4V titanium alloy [J]. Corrosion Science, 2021, 188: 109558.

[24] GUO Wei, WANG Hao, PENG Peng, SONG Bin-wen, ZHANG Hong-qiang, SHAO Tian-wei, HUAN Heng, QIAO Hong-chao, QU Guan-da, ZHU De-zhi, YAN Jian-feng. Effect of laser shock processing on oxidation resistance of laser additive manufactured Ti6Al4V titanium alloy [J]. Corrosion Science, 2020, 170: 108655.

[25] WANG Zhao, HUANG Shu, LU Hai-fei, LIU Jia-jun, ALEXANDROV I V, LUO Kai-yu, LU Jin-zhong. The role of annealing heat treatment in high-temperature oxidation resistance of laser powder bed fused Ti6Al4V alloy subjected to massive laser shock peening treatment [J]. Corrosion Science, 2022, 209: 110732.

[26] KAN W, CHEN B, PENG H, LIANG Y, LIN J. Formation of columnar lamellar colony grain structure in a high Nb−TiAl alloy by electron beam melting [J]. Journal of Alloys and Compounds, 2019, 809: 151673.

[27] YUE Hang-yu, PENG Hui, LI Rui-feng, YANG Ji-xin, GAO Run-qi, ZHANG Shu-zhi, WANG Xiao-peng, CHEN Yu-yong. Metastable phase and microstructural degradation of a TiAl alloy produced via selective electron beam melting [J]. Vacuum, 2021, 192: 110491.

[28] SUN Ru-jian, CHE Zhi-gang, CAO Zi-wen, ZOU Shi-kun, WU Jun-feng, GUO Wei, ZHU Ying. Fatigue behavior of Ti-17 titanium alloy subjected to different laser shock peened regions and its microstructural response [J]. Surface and Coatings Technology, 2020, 383: 125284.

[29] MA Rui-xin, LIU Zhan-qi, WANG Wen-bo, XU Guo-jian, WANG Wei. Laser deposition melting of TC4/TiAl functionally graded material [J]. Vacuum, 2020, 177: 109349.

[30] LEO J R O, ZABEEN S, FITZPATRICK M E, ZOU J, ATTALLAH M M. A study on the effects of laser shock peening on the microstructure and substructure of Ti−6Al−4V manufactured by selective laser melting [J]. Journal of Materials Processing Technology, 2023, 316: 117959.

[31] PAN Xin-lei, WANG Xue-de, TIAN Zeng, HE Wei-feng, SHI Xiao-song, CHEN Pei-ming, ZHOU Liu-cheng. Effect of dynamic recrystallization on texture orientation and grain refinement of Ti6Al4V titanium alloy subjected to laser shock peening [J]. Journal of Alloys and Compounds, 2021, 850: 156672.

[32] LI N, WANG Y D, LIN PENG R, SUN X, LIAW P K, WU G L, WANG L, CAI H N. Localized amorphism after high-strain-rate deformation in TWIP steel [J]. Acta Materialia, 2011, 59: 6369−6377.

[33] LAN L, XIN R Y, JIN X Y, GAO S, HE B, RONG Y H, MIN N. Effects of laser shock peening on microstructure and properties of Ti−6Al−4V titanium alloy fabricated via selective laser melting [J]. Materials (Basel), 2020, 13: 13153261.

[34] JI Fei-fei, WANG Zhao, WU Liu-jun, LUO Kai-yu, LU Jin-zhong. Strain rate dependence of tensile properties and strengthening mechanism of Ti6Al4V alloy undergoing different coverage layers of laser shock peening [J]. Surface and Coatings Technology, 2022, 447: 128807.

[35] AHMADIKIA B, WANG Le-yun, KUMAR M A, BEYERLEIN I J. Grain boundary slip–twin transmission in titanium [J]. Acta Materialia, 2023, 244: 118556.

[36] ZHANG Xin-yu, LI Chuan-wei, ZHENG Meng-yao, YE Zhen-hua, YANG Xu-dong, GU Jian-feng. Anisotropic tensile behavior of Ti−47Al−2Cr−2Nb alloy fabricated by direct laser deposition [J]. Additive Manufacturing, 2020, 32: 101087.

[37] HUANG Y, PENG X, DONG Z, CUI Y. Thermal growth of

exclusive alumina scale on a TiAl based alloy: Shot peening effect [J]. Corrosion Science, 2018, 143: 76−83.

[38] LI Dong-xu, ZHANG Guo-ying, LU Gang, WANG Jian-jun, LIU Chun-ming. Optimizing high-temperature oxidation behaviors of high-Nb-containing TiAl alloys by addition of boron [J]. Corrosion Science, 2020, 177: 108971.

[39] LIN J P, ZHAO L L, LI G Y, ZHANG L Q, SONG X P, YE F, CHEN G L. Effect of Nb on oxidation behavior of high Nb containing TiAl alloys [J]. Intermetallics, 2011, 19: 131−136.

[40] CAO Jiang-dong, ZHANG Jun-song, HUA Yin-qun, CHEN Rui-fang, YE Yun-xia. Improving the high temperature oxidation resistance of Ni-based superalloy GH202 induced by laser shock processing [J]. Journal of Materials Processing Technology, 2017, 243: 31−39.

[41] LAN Liang, JIN Xin-yuan, GAO Shuang, HE Bo, RONG Yong-hua. Microstructural evolution and stress state related to mechanical properties of electron beam melted Ti−6Al−4V alloy modified by laser shock peening [J]. Journal of Materials Science & Technology, 2020, 50: 153−161.

[42] SUN Ru-jian, CAO Zi-wen, CHE Zhi-gang, ZHANG He-peng, ZOU Shi-kun, WU Jun-feng, GUO Wei. A combined experimental-numerical study of residual stress and its relaxation on laser shock peened SiC particle-reinforced 2009 aluminum metal matrix composites [J]. Surface and Coatings Technology, 2022, 430: 127988.

[43] ZHOU W F, REN X D, REN Y P, XU S D, HUANG J J, YANG T. Laser shock processing on Ni-based superalloy K417 and its effect on thermal relaxation of residual stress [J]. The International Journal of Advanced Manufacturing Technology, 2016, 88: 675−681.

激光喷丸对激光熔化沉积 Ti45Al8Nb 合金显微组织及高温抗氧化性能的影响

蒋露露[1]，兰 亮[1]，白澄岩[1]，辛如意[1]，高 双[1]，汪浩宇[1]，何 博[1]，陈超越[2]，卢国鑫[3]

1. 上海工程技术大学 材料科学与工程学院 高温合金精密成形研究中心，上海 201620；
2. 上海大学 材料科学与工程学院 省部共建高品质特殊钢冶金与制备国家重点实验室，上海 200444；
3. 山东大学 材料科学与工程学院，济南 250061

摘　要：采用激光喷丸(LSP)技术改善激光熔化沉积 Ti45Al8Nb 合金的高温抗氧化性。通过扫描电镜、X 射线衍射和电子背散射衍射等方法研究了 LSP 前后激光熔化沉积 Ti45Al8Nb 合金的显微组织和高温氧化行为。结果表明，在 900 ℃下氧化时，经过 LSP 处理后样品的质量增长率有所下降，表明经 LSP 处理的样品在高温下具有较好的抗氧化性能。LSP 处理后样品中形成了细晶层、变形晶层和粗晶层构成的梯度结构，这有利于氧化过程中 Al 原子的扩散，导致试样表面形成致密的 Al_2O_3 层。最后，探讨了 LSP 技术提升激光熔化沉积 Ti45Al8Nb 合金抗氧化性能的机理。

关键词：TiAl 合金；激光熔化沉积；激光喷丸；增材制造；抗氧化性

(Edited by Bing YANG)